SAND2024-00121

SANDIA REPORT

Printed January 2024

Sandia National Laboratories

MASK4 Test Report

Dominic D. Forbush, Ryan G. Coe, Tim Donnelly, Giorgio Bacelli, Damian Gallegos-Patterson, Steven J. Spencer, Johannes Spinneken, Jantzen Lee, Robert Crandell, Kevin Dullea

Prepared by
Sandia National Laboratories
Albuquerque, New Mexico 87185
Livermore, California 94550

Issued by Sandia National Laboratories, operated for the United States Department of Energy by National Technology & Engineering Solutions of Sandia, LLC.

Available to DOE and DOE contractors from

U.S. Department of Energy
Office of Scientific and Technical Information
P.O. Box 62
Oak Ridge, TN 37831

Telephone: (865) 576-8401
Facsimile: (865) 576-5728
E-Mail: reports@osti.gov
Online ordering: http://www.osti.gov/scitech

Available to the public from

U.S. Department of Commerce
National Technical Information Service
5301 Shawnee Road
Alexandria, VA 22312

Telephone: (800) 553-6847
Facsimile: (703) 605-6900
E-Mail: orders@ntis.gov
Online order: https://classic.ntis.gov/help/order-methods

ABSTRACT

Wave energy converters (WECs) are designed to produce useful work from ocean waves. This useful work can take the form of electrical power or even pressurized water for, e.g., desalination. This report details the findings from a wave tank test focused on that production of useful work. To that end, the experimental system and test were specifically designed to validate models for power transmission throughout the WEC system. Additionally, the validity of co-design informed changes to the power take-off (PTO) were assessed and shown to provide the expected improvements in system performance.

Acknowledgment

Our team would like to thank Miguel Quintero, Samantha Lee, Andrew McCoy, and the many other people at the Naval Surface Warfare Center, Carderock Division for their expertise and hard work.

CONTENTS

LIST OF FIGURES

LIST OF TABLES

1. INTRODUCTION

This report describes the "MASK4" wave tank test of the Sandia WaveBot device. The WaveBot device has been tested a number of times in different permutations at the US Navy's Manuevering and Sea Keeping (MASK) basin. Each test in this series is referred to as MASK1, MASK2, etc. The WaveBot device was first tested in one degree of freedom (heave) in 2016 [14, 5, 3]. This MASK1 test focused primarily on system identification and modeling. After MASK1, major modifications were performed to improve the overall real-time control and measurement system, improve the heave drive train, and add surge and pitch degrees of freedom. The second set of testing, which was broken up in to two stages: MASK2A and MASK2B, focused on bench testing and closed loop control performance [15, 6, 10, 11] as well as nonlinear modeling [9]. MASK3 then focused on multi-input, multi-output modeling and control for maximization of electrical power [16]. A summary report [13] provides a summary of this work as well as related efforts. This report presents the results from MASK4, which focuses on detailed modeling of the power conversion chain and validation co-design principles by way of the introduction of a magnetic spring.

This report is intended to be accompanied by an open-source dataset and set of MATLAB scripts.[1] The report provides high-level takeaways, while referencing relevant MATLAB scripts and data files that can be used to further explore the results. Figure captions reference relevant MATLAB scripts that can be used to reproduce their results.

[1] See `https://github.com/sandialabs/fbWecCntrl/tree/master/MASK4`.

2. BACKGROUND

The "intrinsic impedance," which captures the devices hydrodynamics, is defined as (see, e.g., [17])

$$Z_i = B_h(\omega) + j\left(\omega\left(M + A_h(\omega)\right) - \frac{K_h}{\omega}\right). \tag{2.1}$$

Here, $B_h(\omega)$ and $A_h(\omega)$ are the hydrodynamic radiation damping and added mass The hydrostatic restoring stiffness is K_h and M is the rigid body mass. In practice, the individual terms in (2.1) can be determined numerically/analytically or one may estimate Z_i from empirical testing [5]. For a given wave excitation force (F_e) and a PTO force (F_{PTO}), the WEC response will be

$$Z_i\, V = F_e - F_{PTO} \tag{2.2}$$

Figure 2-1 shows a two port network diagram that can be used to represent a WEC's power transmission dynamics. Here, we consider a linear impedance Z relating *effort* (e) and *flow* (q).

$$e = Zq \tag{2.3}$$

For our system illustrated in Figure 2-1, this takes the form of

$$\begin{bmatrix} F_{PTO} \\ V_{out} \end{bmatrix} = \begin{bmatrix} Z_{11} & Z_{12} \\ Z_{21} & Z_{22} \end{bmatrix} \begin{bmatrix} v \\ i_{out} \end{bmatrix}, \tag{2.4}$$

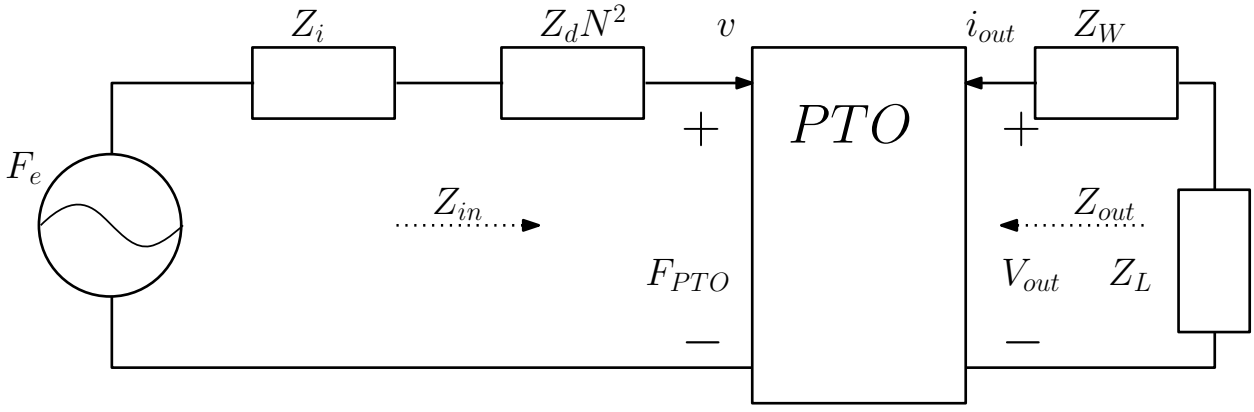

Figure 2-1. Two port network diagram representing wave energy converter power transmission system.

where the *effort variables* are the PTO force (F_{PTO}) and the output port's voltage (V_{out}). The *flow variables* in (2.4), that result from the effort variables, are the velocity (v) and output port's current (i_{out}). In the case of the WaveBot, the elements of Z are defined as

$$Z = \begin{bmatrix} Z_{11} & Z_{12} \\ Z_{21} & Z_{22} \end{bmatrix} = \begin{bmatrix} Z_d\, N^2 & -\sqrt{\frac{3}{2}} K_t\, N \\ \sqrt{\frac{3}{2}} K_t\, N & Z_w \end{bmatrix} \tag{2.5}$$

where N is the gear ratio, K_t is the motor/generator torque constant (N-m/A) and Z_w is the winding impedance of the motor/generator (hereafter shortened to motor, for brevity).

$$Z_w = R_w + j\omega L_w \tag{2.6}$$

Here, R_w and L_w is the motor resistance (Ohm) and inductance (H) respectively. The term Z_d is the drivetrain impedance, describing the ratio between output force and input velocity between the motor/generator shaft and the buoy (i.e., the dynamics of the PTO that are not affected by system hydrodynamics). Expressed as a second-order mass-spring-damper system,

$$Z_d = j\omega M_d + B_d + \frac{K_d}{j\omega} \tag{2.7}$$

where M_d, B_d, and K_d are the effective drivetrain inertia, damping, and stiffness, respectively.

As shown in Figure 2-1, we may consider the input and output impedances of the PTO, which relate the effort and flow variables on each of the respective ports (input and output). For the input impedance, we consider the ratio of the input port effort and flow variables (F_{PTO} and v, respectively) in a scenario when the input port is open (disconnected) and with the output port connected fully so that $V_{out} = -Z_\ell i$.

$$Z_{in} = \frac{F_{PTO}}{v} = Z_{11} - \frac{Z_{12}\, Z_{21}}{Z_{22} + Z_\ell} \tag{2.8}$$

Here, Z_ℓ is the load impedance, which, in the context of this test, is the controller applied to the motor actuating the WEC heave degree of freedom. The input impedance Z_in describes the dynamics of the system as seen by, but excluding, the buoy: in theory, the buoy hull could be replaced with a completely new hull, but the input impedance would remain the same. Similarly, for the output impedance, we consider the ratio of the out port effort and flow variables (V_{out} and i_{out}, respectively) in a scenario where the out port is open and the in port is fully connected ($F_e - F_p = Z_i v$), but with the excitation set to zero ($F_e = 0$). The output impedance Z_{out} describes the dynamics of the system as seen by, but excluding, the load.

$$Z_{out} = \left.\frac{V_{out}}{i_{out}}\right|_{F_e=0} = Z_{22} - \frac{Z_{12}\, Z_{21}}{Z_{11} + Z_i} \tag{2.9}$$

In theory, the load could be replaced with another, but the output impedance would remain the same.

Maximum power transfer to the load requires satisfaction of a biconjugate impedance matching condition.

$$Z_{in} = Z_i^* \tag{2.10a}$$
$$Z_{out} = Z_\ell^* \tag{2.10b}$$

Note that the conditions specified by (2.10) are dependent on the intrinsic impedance that captures the hydrodynamics as well as the elements of the PTO impedance as defined by (2.5) and the load impedance. Thus, for a given intrinsic impedance, we may best satisfy (2.10) by appropriate design of *both* a controller and the PTO.

3. METHODS

3.1. Device description

A diagram of the WaveBot is shown in Figure 3-1 The MASK4 version of the WaveBot is similar to previously tested iterations (see, e.g., Section 1), with three key changes discussed in the subsequent sections.

3.1.1. Controlled degrees of freedom

The WaveBot was previously tested with three (heave, surge, and pitch) degrees of freedom, all controlled to maximize power absorption. For MASK4, only the heave degree of freedom was studied for power absorption. The pitch degree of freedom was removed (i.e., pitch motion was locked out) and the surge degree of freedom was controlled to act in a purely passive load reduction mode (similar to a mooring system).

3.1.2. Magnetic spring

Based on co-design findings [4, 21, 18] and numerical modeling, a tunable magnetic spring developed by Portland State University [8, 7, 20] was added to the heave PTO system. Figure 3-2 illustrates degrees of freedom of the magnetic spring. By moving the stator axially into or out of the rotor, the effective spring rate for the rotational motion of the rotor is altered. This magnetic spring and the WaveBot's electrical motor act in parallel. A Nanotec PD4-EB59CD-M-65-1A actuator, a GPLE60-2S-25 gearbox, and VT320-06-CR-E-U1-20-C02 actuator were employed to move the magnetic spring's stator axially through the rotor, allowing the torsional restoring effect of the spring to be modulated. Photographs of the installed magnetic spring system are shown in Figure 3-3.

3.1.3. Power measurement

Mechanical and electrical power was measured at different stages in the PTO system. Figure 3-4 shows a schematic of power measurement locations on the WaveBot. The mechanical power on the vertical tube ($P_{mech,1}$) is the product of linear velocity (heave encoder velocity, field name `heaveSignals.heaveEncVel_m_s`) and force (heave column load cell, field name `heaveSignals.heaveForceLCB_N`). The mechanical power on the motor shaft ($P_{mech,2}$) is the product of rotational velocity (heave encoder velocity, field name `heaveSignals.heaveEncVel_rad_s`) and torque (heave motor shaft load cell, field name `heaveSignals.heaveForceTRS_N_m`). Note

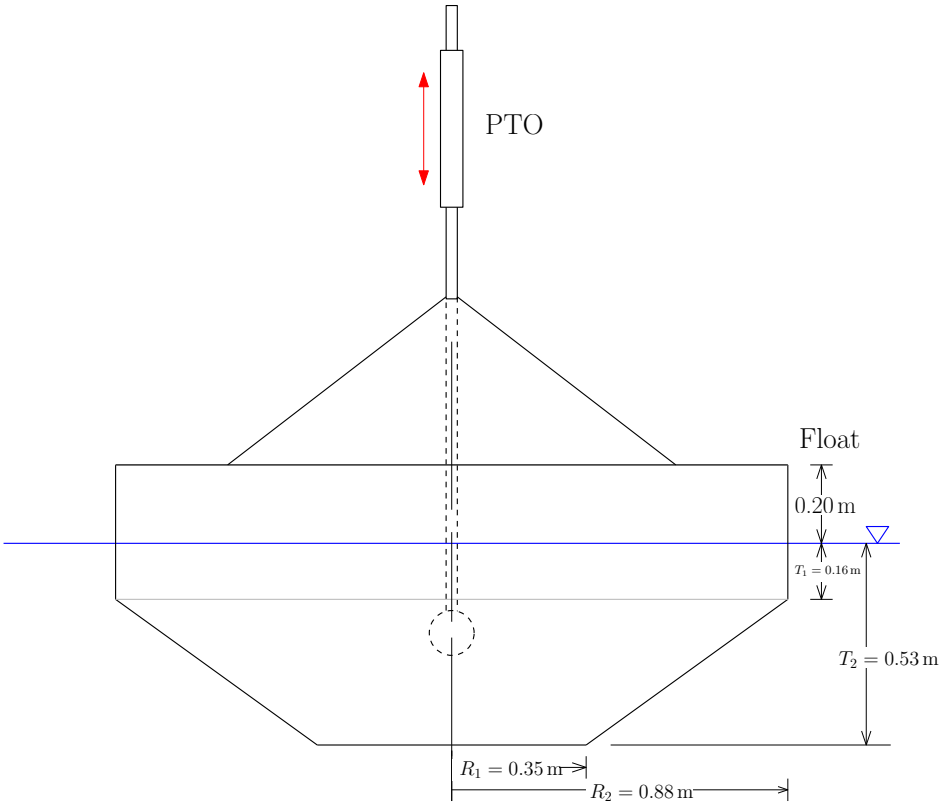

Figure 3-1. WaveBot device diagram.

that this is given equivalently in the linear frame using `heaveSignals.heaveForceTRS_N` and `heaveSignals.heaveEncVel_m_s`, as these are calculated from the measurements taken in the rotational frame using the appropriate gear ratios. The alternating current electrical power between the motor and the motor controller ($P_{elec,AC}$) is calculated by an HBM power analyzer measurement as the sum of the powers in the three phases of AC leads connect to the motor (field name `hbmSignals.heaveDriveOutSumP`). The power on the direct current (DC) bus ($P_{elec,DC}$), which is considered the "delivered power" in this system, is the also measured at the HBM as the DC power out of the drive towards the DC bus (field name `hbmSignals.heaveDriveInP`).

3.1.4. Custom motor drive

The WaveBot PTO was initially designed with the goal of providing accurate torque tracking (i.e., the PTO should be able to produce a requested torque trajectory). As part of this design, a commercial off-the-shelf (COTS) motor drive from Advanced Motion Controls (DPEANIU-C100A400) was used [2]. However, work at Monterey Bay Aquarium Research Institute (MBARI) [19] has shown the potential benefit of tailoring the motor drive to the WEC PTO application. Further research has confirmed that simply altering the firmware for existing motor drive hardware has the potential to provide large efficiency gains for WECs [23].

Thus, a COTS inverter (SPM-VFDHP [22]) paired with custom firmware was added to the heave PTO drive train for further proof of concept testing of these ideas. A diagram of the custom control

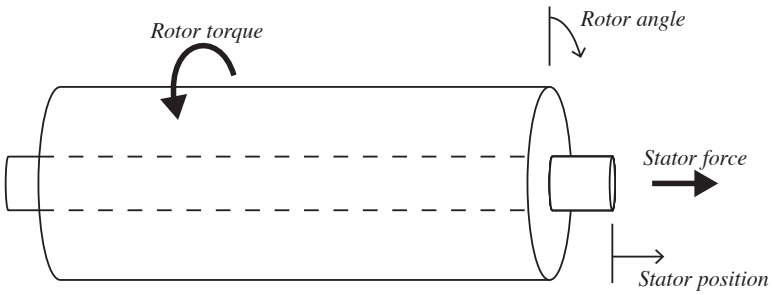

Figure 3-2. WaveBot PTO with magnetic spring degrees of freedom.

firmware is shown in Figure 3-5. The variables which were adjusted to study their impact on drive efficiency are: DC bus voltage, inverter switching mode, inverter switching frequency, velocity threshold, and current hysteresis threshold. The latter two are control that use logic to temporarily disable the drive when the velocity of the motor is less than a specified threshold (m/s) [23] or defines the deadband on drive current control (A), respectively.

3.1.5. Wave Measurement

Basin wave measurements are described in detail in [16]. The wave series number corresponds to a file name in the basin-provided data set (files ending in a *.twe extension). Note that although the data collection times are synchronized via GPS time servers, the WaveBot filenames (e.g., `waveBotCtrlMdl_2023_09_22_08_47_32.mat`) and the start time given in the corresponding AWDC (a wave basin naming convention) wave log (e.g., wave series 10 start time of 1114) are based upon two distinct wall clock times: the start time reported in the AWDC wave log leads the WaveBot file name time stamp by approximately 2 hours and 20 minutes. This wave data has been read into the WaveBot data structure using 3 codes `tweRead.m`, `tweSync.m`, and `tweMerge.m`. `tweRead.m` loads a data table with all wave data and wave DAQ elapsed time. The script `tweSync.m` calculates two additional synchronized time series, each by a unique method, to align wave data acquisition elapsed time with waveBot elapsed time. The first aligns the wave time to waveBot time by synchronizing the transistor-transistor logic (TTL) data acquisition signal to the nearest 50 Hz sample. The second uses the TTL-aligned time as an initial guess, and then aligns more precisely over the period of interest by lagging the wave time series by an amount that maximizes the cross-correlation between a 1 Hz sine wave generated and read by the waveBot DAQ with the same sine read by the wave DAQ. This is more precise in that the correlation occurs at the higher (200 Hz) sampling rate, but fundamentally different in that this synchronization method optimizes correlation over the period of interest, not just a single point in time, as is the case with the TTL synchronization method.

Users of the MHKDR data upload will not interact directly with the *.twe files: basin provided data has already been merged and synchronized into the available data structures.

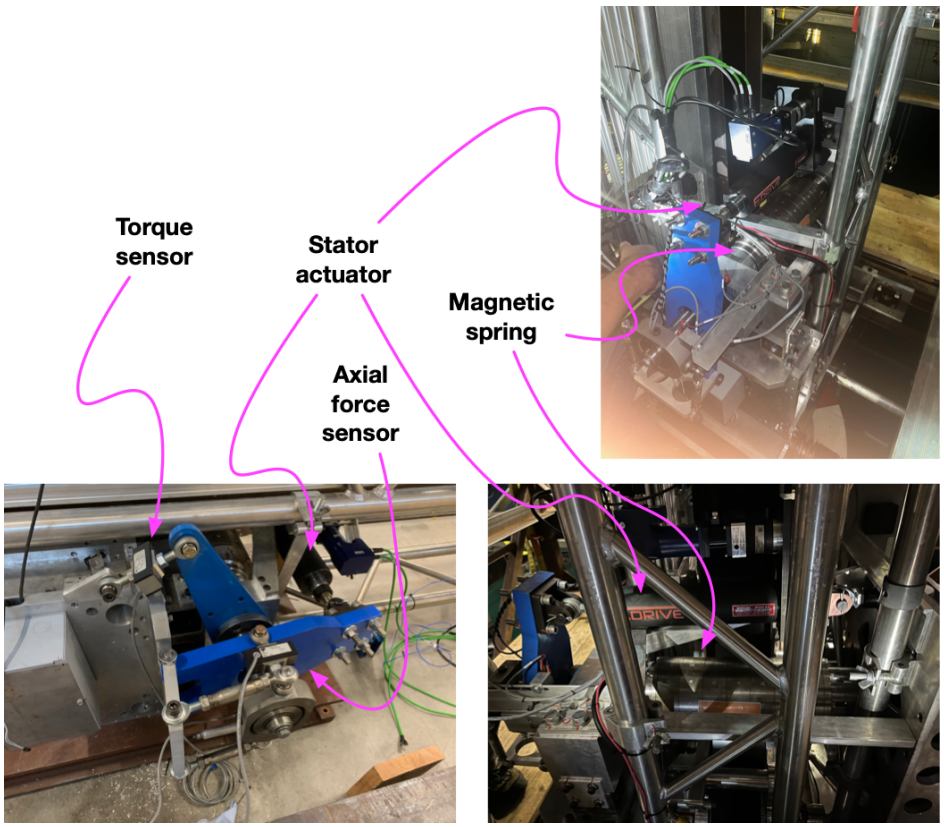

Figure 3-3. Magnetic spring installed with sensors.

3.2. Test types

Two major categories of tests were conducted for this effort:

- **Open-loop tests:** Open-loop tests, in which actuator signals were defined by pre-calculated trajectories, were performed primarily for SID and performance mapping. Typically, open-loop test actuator signals were defined by either single frequency sinusoids or band-limited periodic ("multi-sine") signals. These tests were conducted in calm water ("radiation tests") and in cases with waves.

- **Closed-loop tests:** Closed-loop tests, in which actuator signals were determined by some combination of feedforward and feedback logic, were performed to assess performance and validate numerical simulations. Waves for these closed loop tests were either single frequency "regular" waves or idealized ocean spectra ("irregular waves") – see Table 3-1 for a listing of irregular wave conditions. Note that all ocean spectra were realized as periodic signals with a repeat period of 5 minutes to facilitate efficient assessment of performance based on multi-dimensional test matrices of different magnetic spring rates, feedback control gains, and motor drive settings.

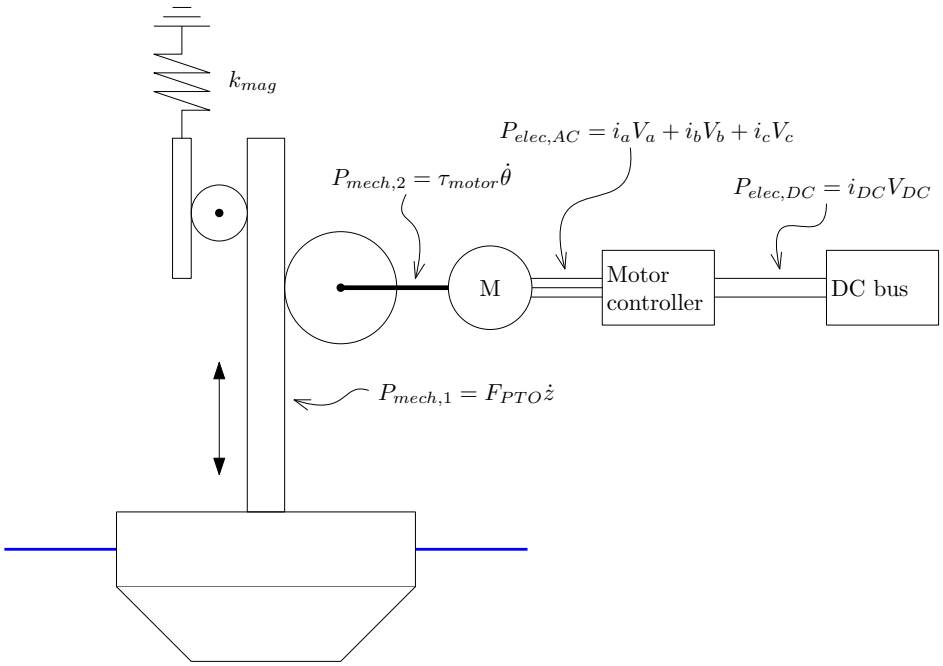

Figure 3-4. MASK4 WaveBot power measurement locations.

Table 3-1. List of irregular wave JONSWAP spectra conditions that were evaluated in MASK4 Basin tests.

Sig. Height (m)	Peak Period (s)	γ
0.127	3.45	3.3
0.127	2.5	3.3
0.254	2.5	3.3
0.127	1.58	3.3
0.254	1.58	3.3

3.2.1. Device Characterization

3.2.1.1. Magnetic Spring

The MASK4 WaveBot was equipped with a tunable magnetic spring that adjusts the natural resonant frequency of the buoy-drivetrain system, and can provide a negative spring stiffness. To characterize this spring, the stage was moved throughout its full range of motion using a chain hoist. Considering small angular displacements, the effective spring rate is a function of stator position. To characterize these spring rates as a function of stator position, the device was raised and lowered through its full range of motion using a chain hoist for a variety of stator positions.

The resonant frequency of the system (Hz) can be approximated as

$$f_n = \frac{1}{2\pi}\sqrt{\frac{K_h + K_s}{A_\infty + m}}, \tag{3.1}$$

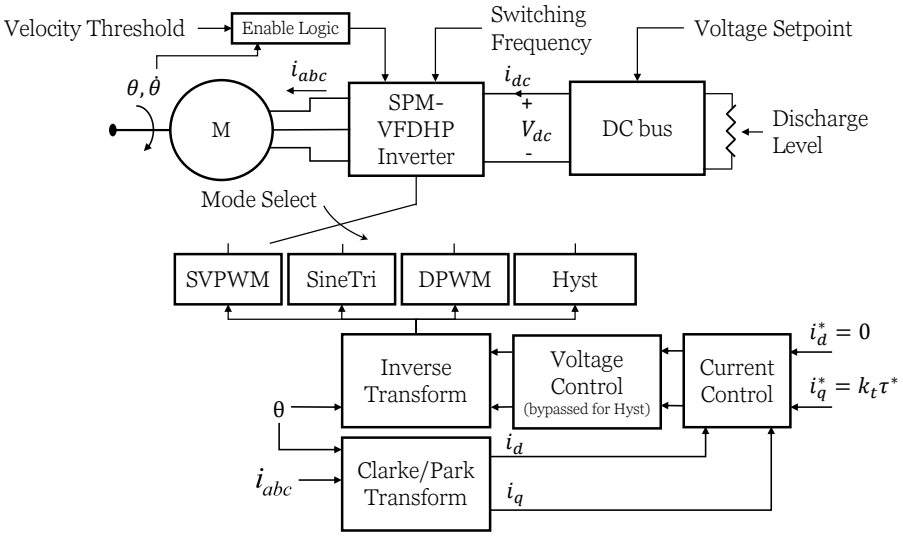

Figure 3-5. Heave custom drive hardware configuration and associated controls.

where K_s is the spring rate contributed by the magnetic spring (N/m), A_∞ is the infinite frequency added mass of the buoy (kg), and m is the static mass of the buoy and heave stage assembly.

3.2.1.2. Surge Damping Determination

The only degree of freedom of interest for power capture in this test campaign is heave. Device actuation in surge was considered analogous to a mooring and was tuned to restrict surge displacement to a safe range (i.e., station-keeping) without adversely affecting power capture. To achieve this the buoy was subjected to 0.5 Hz regular waves, near the surge resonant frequency at the maximum positive magnetic spring setting. The surge proportional gain (damping) was adjusted manually so that the range of motion was within safe limits while maintaining high power capture. The determined value for surge damping was 2500 N-s/m and this was used for all wave tests except for some tests of the custom drive, which are explicitly noted in the test log.

3.2.2. System Identification

A family of linear admittance models were identified for a set of magnetic spring positions to determine the intrinsic admittance Y_i (the inverse of intrinsic impedance Z_i) and the drivetrain admittance Y_d (the inverse of drivetrain admittance, Z_d). The system identification approach followed the method of [5], using two unique phase realizations of a multisine excited between 0.2 and 1 Hz with a repeat period of 300 s. A minimum of two periods were calculated for each test. This procedure was repeated for three amplitudes of motion, measured by the maximum amplitude of the current command on the actuated multisine: 10, 20, or 30 A. Thus, for each spring position, six tests were completed, and three 1-DOF models were identifed, once at each amplitude.

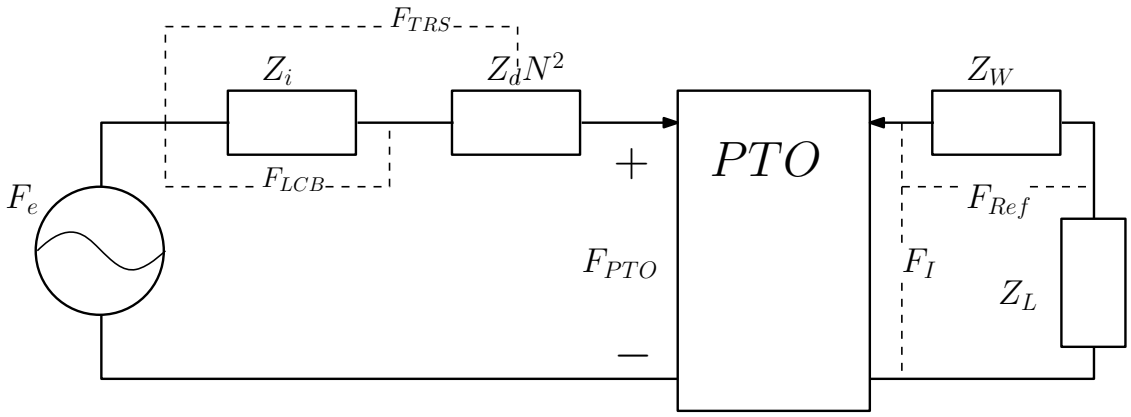

Figure 3-6. The effort variables in the 2-port impedance model measured by various force sensors, indicated by the dashed lines. On the right hand side of the PTO block, the effort variable is electrical current, but this has been converted to a force via calculation from motor properties to align with the WEC side of the PTO, and is annotated accordingly. In post-processing, F_{TRS} is converted from the rotational torque measurement and, though it includes all relevant drivetrain dynamics, is presented on the same side of the gearbox as F_{LCB}.

From these identified impedance models, a frequency domain estimation of excitation was determined from a subsequent test in which the multisine actuation was repeated at 20 A in the presence of pink-spectrum waves excited over the same 0.2 to 1 Hz frequency band with a repeat period of 300 s. Three separate phase realizations of this pink wave were completed. Following [5], the frequency domain excitation f_{exc} (N/m) relating empty-basin wave height η (m) to excitation force in heave F_{exc} (N)

$$f_{exc} = \frac{F_{exc}}{\eta} \tag{3.2}$$

can be calculated from the intrinsic impedance Z_i (the inverse of intrinsic admittance, Y_i) and the frequency-domain buoy velocity Ω as

$$f_{exc} = \frac{\Omega Z_i - F_{PTO}}{\eta} \tag{3.3}$$

where the empty-basin wave height is determined by running an identical pink-spectrum wave with a wave probe placed at the nominal WEC location prior to WEC installation in the basin. This wave calibration test was performed in a previous test campaign, described in [15]. The sensor 'BUOY04' was used for this calibration because, although 'BUOY05' is slightly closer to the nominal WEC location, the spectral content of the 'BUOY05' wave height data was nearly zero at several included frequencies, resulting in near-singularities at these values.

Note also that because this wave calibration data is from a previous test campaign, a version of the legacy script `importNSWCCD.m` is included and should only be used to load the included calibration data. The basin wave data from the current test can be imported using the `tweRead.m`, `tweSync.m`, and `tweMerge.m` scripts. However, because this wave data all was taken while the device was in the basin, it contains waves reflected and radiated from the WEC which should not be included in the excitation wave estimate η in (3.3).

3.2.3. Power Surfaces

Of primary interest during this test campaign is the influence of heave controller parameters K_P and K_I, which affect the load impedance Z_L, and magnetic spring setting K_s, which affects drivetrain impedance Z_d, on the power capture of the WEC device. Particularly, mechanical power absorbed by the buoy, AC electrical power delivered to the motor drive, and DC electrical power exported from the motor drive are of interest. To develop these power surfaces for a given sea state, a given combination of parameters was held for 20 s (for all regular waves) or 300 s (for all irregular waves), before switching to another set of parameters. The order of parameter combinations and the time of switching events was controlled by the gain matrix (as noted in the test log) utilized for that particular test.

For any sea-state, a mechanical, AC electrical, or DC electrical power surface can be determined by averaging the measurements described in Section 3-4 over an integer number of periods (for regular waves, for which multiple periods were available between 20 s switching intervals) or a single period (for irregular waves, which have a repeat period equal to 300 s switching interval). It should be noted that gain matrices typically have several additional rows that are intended to eliminate transients associated with wave start-up or a set point change or to facilitate data processing. This includes a first row entry maintained for a short interval, typically 5 s, followed by a second row entry identical to the third row held until 120 s and 20 s, respectively. The change between the first and second row is necessary to initially load the intended parameter combination, and the lengthy delay between the second and third rows is intentional so that the desired sea state (initiated at time zero) will be fully achieved in the basin by the time of the third row. Processed data thus discards the first two rows. Additionally, when the magnetic spring changes positions, a parameter combination will be repeated for an additional switching interval so that data taken while the spring set point was changing, which takes several seconds, could be discarded without loss of fidelity. Finally, the last row of many gain matrices makes $K_p = -999$: data beyond this point is discarded, serving as a signal to the operator and the data processing scripts that the test is over. In the processing scripts used to produce the power surfaces, these rows are skipped deliberately.

In the provided data structures, the fields `heaveSignals.heaveKpUsed`, `heaveSignals.heaveKiUsed`, and `magSpringSetpointSignals.targetSpring_N_m` contain the utilized K_P, K_I, and K_s values, respectively. Absorbed electrical AC and DC power measurements are contained in the `hbmSignals` field.

3.2.4. Custom Drive

Similar to the above tests, power capture is a variable of interest in the investigation of the custom drive. While the wave excitation and analysis was conducted identically, these tests differ from those conducted with the standard drive in that drive parameters such as switching time, velocity switching threshold, and DC bus voltage were varied additionally to heave controller and magnetic spring parameters (Table 3-2). Parameters varied changed from test-to-test, as described in the test matrix and the associated gain matrix. Note that for some of these tests, the heave control gains do not in fact vary: however we continue to describe the parameter-controlling file as a gain matrix for consistency.

Table 3-2. List of tested drive switching schemes and their varied parameters

Switching mode	Varied Parameters	Test IDs
Space-vector pulse width modulation (SVPWM) [1]	dcBusVoltage, driveSwitchT, driveVelThreshold, dischargeLevel	109, 111, 112, 113, 116, 117, 118, 119, 120, 124, 125, 126, 132, 133, 135, 136, 138, 139
Discontinous pulse width modulation (DPWM) [12]	dcBusVoltage, driveSwitchT, driveVelThreshold	110, 122, 127, 137
Sine-triangle PWM (SineTri) [1]	dcBusVoltage, driveSwitchT, driveVelThreshold	121
Hysteresis current control (Hyst) [1]	dcBusVoltage, driveHystTol, driveVelThreshold	123

Table 3-3. Description of drive parameters

Varied Parameters	Description
dcBusVoltage	The set point DC bus voltage. With the power supply on, this value will not decrease substantially below this value. Above this value, the discharge circuit is intended to open to maintain this value.
driveSwitchT	The switching period of the drive PWM, in seconds.
driveVelThreshold	The WEC velocity (m/s) above which the drive will turn on.
driveHystTol	The hysteresis deadband on drive current control (A), used for the hysteresis switching scheme, unused otherwise.
dischargeLevel	A binary value: 1 for one of the parallel discharge resistors connected (maximum resistance) and 15 for all parallel resistors connected (minimum resistance).

Because the custom drive efficiency was sufficient to capture electrical power, the DC bus voltage was set to discharge through dump resistors above a certain voltage (set manually to be slightly higher than nominal), with this circuit opening again when bus voltage decreased below a manually-set value slightly lower than nominal. Second, the internal PWM set points are obtained by a drive proportional-integral that is controlled by gains that are unique from WEC K_p and K_i gains: these drive parameters are tunable, but were found to be sufficient for the included investigations and therefore are not varied in the test runs (or presented in Table 3-2). Additionally, for some runs in sufficiently energetic sea-states, the WEC power supply was disconnected so that the WEC operations were maintained from captured wave energy and the charged capacitor bank. This is not expected to affect WEC dynamics at all, but is noted in the test log as the effect upon some electrical sensors is significant.

In the provided data structures, custom drive parameters are contained in the field `toDriveSGSignals`, and measurements performed at the custom drive are contained in the field `fromDriveSGSignals`. Absorbed AC and DC electrical power measurements are contained in the `hbmSignals` field.

4. RESULTS

Conducted tests can be broadly grouped as device characterization, power surface mapping, and custom drive parameter variations. Supporting codes that can recreate the presented plots using what has been made available on MHKDR are provided throughout this section.

4.1. Device characterization

The resulting surfaces for the torque and stator force of the magnetic spring are shown in Figure 4-1. The linear spring stiffness for a given stator position was estimated as the slope of the line of best fit over the linear region defined post-hoc as ±40° of magnetic spring rotation, or ±0.3 m of linear heave travel (see Figure 4-2). Note that stator force, at the extremes of motion for smaller-magnitude spring rates, changes sign. To avoid fatigue loads during wave operation, large displacements were avoided for stator positions in which this force reversal was significant (see Figure 4-3).

The resulting stator position to spring rate map is given in Table 4-1 and Figure 4-4. Note that a gear ratio was accidentally omitted in this calculation initially, so the spring rate that was presumed for all runs prior to 51 must be multiplied by 0.7690 to be accurate. For example, the reported spring rate of -12,000 N/m for run 24 is in fact -9,228 N/m, but the reported spring rate of -6,152 N/m for run 62 is accurate.

The magnetic spring can augment the natural system resonance of 0.65 Hz between a range of 0.73 Hz at the maximum positive spring rate and 0.48 Hz at the maximum negative spring rate.

The script `magSpringMapping.m` can recreate all but the first figure of this section, these figures are obtained by selecting X-Y and X-Z views of the first figure.

Table 4-1. The small-displacement heave spring rate corresponding to various magnetic spring stator positions.

Stator position (%)	Linear spring rate (N/m)
-93	8340
-73	7670
-53	5873
-33	3379
-13	490.9
7	-2763
27	-5715
47	-8508
67	-10013

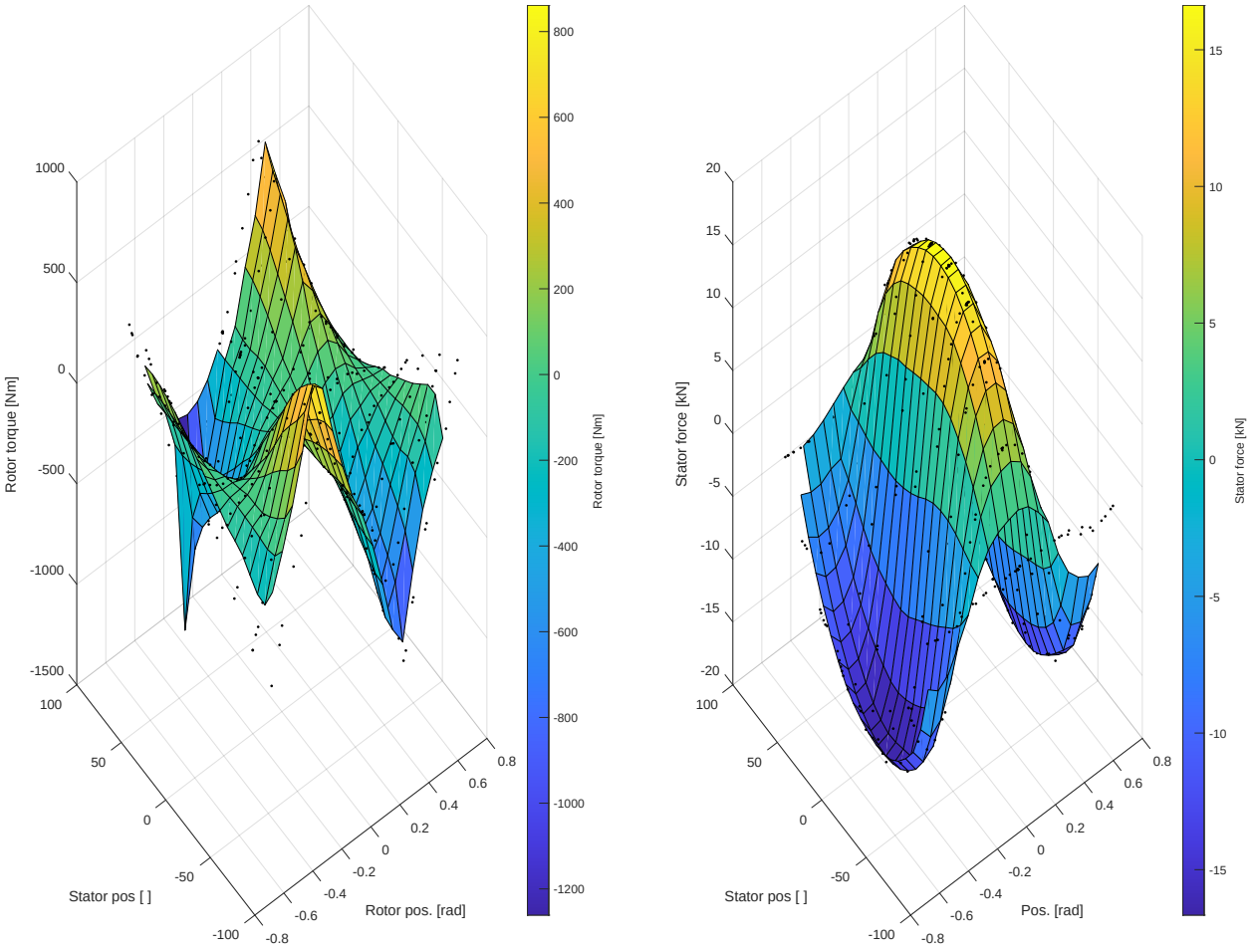

Figure 4-1. Surfaces for magnetic spring rotor torque (left) and stator force (right) as a function of rotor and stator position. Black dots show individual measurements. (MATLAB file: `MASK4_mag_spring_mapping.m`)

4.2. System Identification

The intrinsic and drivetrain impedance of the device was characterized in both heave and surge through multi-sine actuation of the individual degrees of freedom at three distinct amplitudes, following the suggested procedure in [5]. This was carried out for a variety of magnetic spring settings. Upon installation of the custom drive, one such setting was repeated to verify that relevant system dynamics were unchanged.

While encoder-measured velocity was the consistent output of interest, four unique inputs were considered: the force command, the force calculated from the drive-measured current, force measured from driveshaft-mounted TRS load cell, and force measured by the LCB load cell. The first three are nearly redundant measures of drive-delivered force, only differing by the drive current-tracking dynamics, which are not significant at these frequencies of interest (Figure 4-5). The latter LCB load cell measures the buoy forces. While the former three lead to similarly nearly identical estimates of the series $Y_i Y_d$ system (abbreviated Y_{id} in supporting codes), while the latter system identification estimates Y_i. Most significantly the identified Y_i system does not vary with

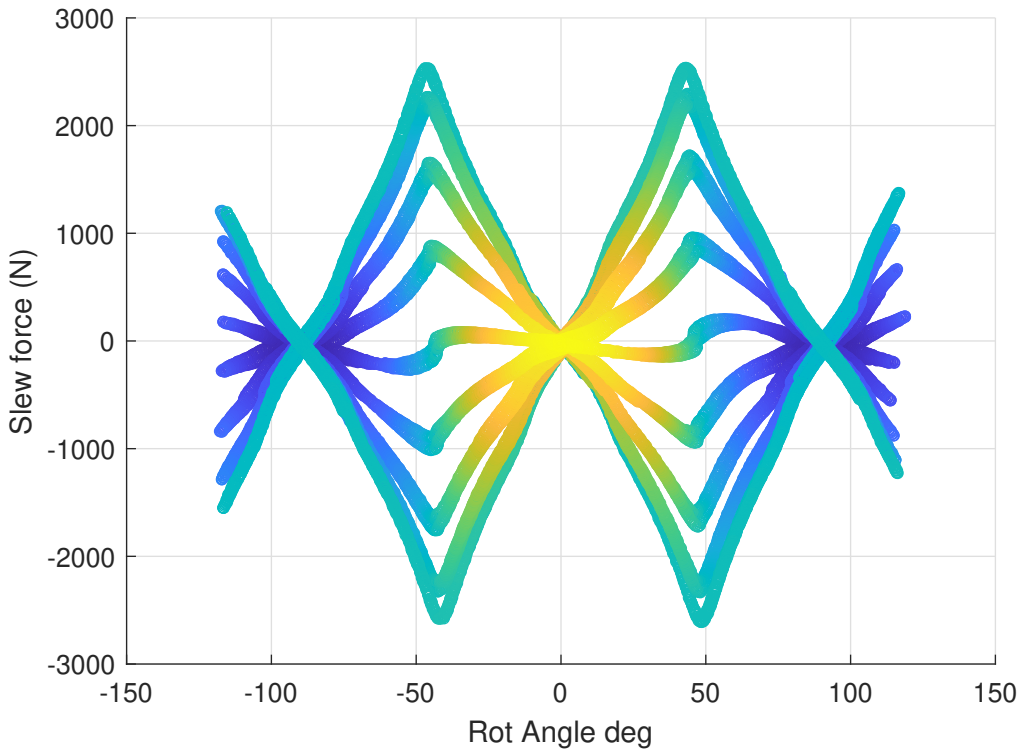

Figure 4-2. The X-Y view of the 3-D surface plot, relating slew force (N) to rotor angle (deg). The small displacement spring rate is estimated from the slope of a linear fit between $\pm 40^{\circ}$ for each stator position setting and is clearly visualized in this plot.

magnetic spring settings (Figure 4-6). Y_d can then be calculated from the identified series system (Figure 4-7).

An issue with the LCB load cell linkage was noticed on the morning of 9/26 that was causing the LCB load cell signal to have slightly elevated levels of noise. Runs after MASK053 have an improved signal. The distinction in identified systems, however, is negligible. The first plot in this section can be recreated from the MHKDR materials by running `msSysIdentification1x1heave.m`.

The wave excitation model for the device is not used to determine control settings or advise other tests, but may be useful for simulations or to validate the excitation coefficients estimated from boundary element methods. This is calculated using the non-parameteric Y_i and Y_d models identified above and calibrated pink-wave height, resulting in the following excitation model (Figure 4-9). Note that the identified model, on average, predicts slightly less excitation that than BEM. The large peaks in this model are due to low observed amplitudes of the nominally pink wave spectra, which results in the division by a small number in Equation 3.3.

This figure can be recreated from the MHKDR materials by running `calcExcitationv3`.

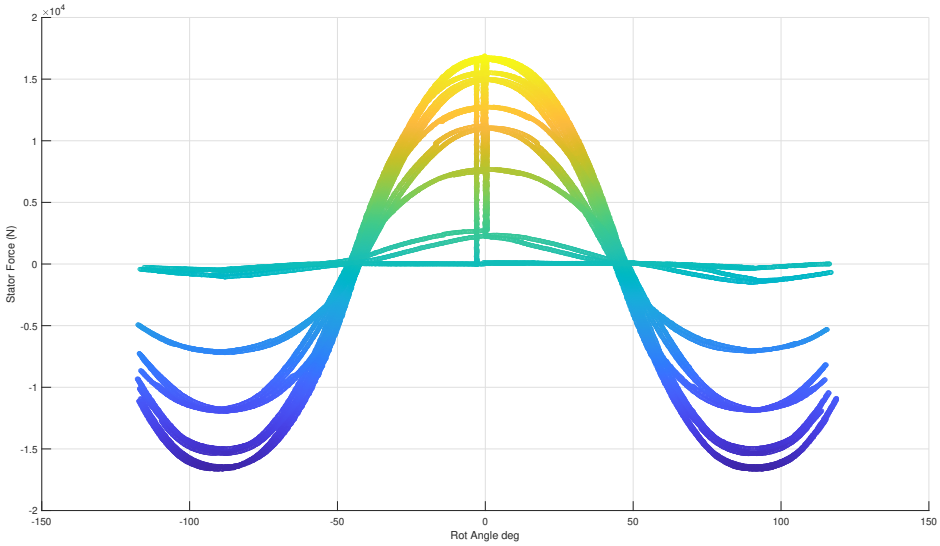

Figure 4-3. The X-Z view of the 3-D surface plot relating the stator force (N) to rotor angle (deg). A stator force that changes sign is undesirable for system fatigue, and the small magnitude spring rate settings were limited to small-displacement operations to avoid this.

4.3. Power Surfaces

For a variety of both regular and irregular waves, a selection of controller (proportional and integral) gains and magnetic spring settings were attempted. To visualize these surfaces, they are sliced at the power-maxima in question of the excluded variable. For example, for a test that varied K_p, K_i, and K_s, a surface displaying the AC electrical power surface as a function of K_p and K_i is evaluated at the value of K_s containing the AC power optimum. By convention, useful power absorbed is negative (i.e., it is desirable to *minimize* power). There are significant differences between DC and AC side power captures using the commercial AMC drive because there is a large parasitic current draw: particularly for cases where there is little AC power available, this can cause DC and AC power optima to occur for substantially different gain values, highlighting the significance of the motor drive dynamics and power consumption in optimal WEC co-design.

Of significance to the two-port model impedance matching criteria, approximately identical combinations of integral gain and magnetic spring settings were attempted. These both act as negative-spring type elements dynamically, but affect different terms of the two port model: the magnetic spring affects the imaginary part of Z_d, while the integral control gain affects the imaginary part of Z_L, and they therefore have unique impacts on the impedance matching conditions resulting in unique power captures.

Because of some non-linear behavior of the magnetic spring, a particular value of spring rate setting was not dynamically identical to the same value applied to as an integral control gain, but the trends in terms of impedance matching conditions are nonetheless obvious. Note especially that for an approximately similar effective spring rate ($K_i - K_s$), the mechanical power surfaces for both magnetic spring rates are similar, but AC and DC power surfaces both differ substantially.

When utilizing the MHKDR resources, test matrices that describe a uniform grid without repeated

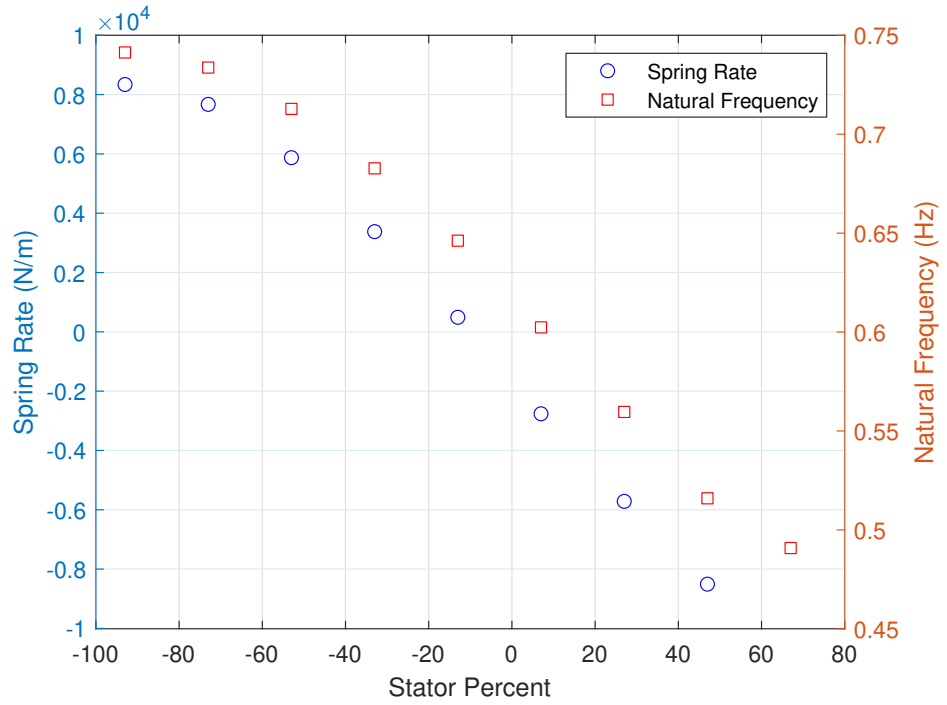

Figure 4-4. Magnetic spring small-displacement linear spring rate map, and the anticipated natural frequency of the system.

points can be analyzed by `makePowerSurfacesv2.m`, as the subfunction relied upon therein for plotting `makeSurfacePlots.m` presumes uniform grids. For non-uniform grids, or those with repeated points, `makePowerSurfacesv3.m` should be used, though the indices of the variable excluded from the plot axis (in this case, magnetic spring rate) must be specified for each run.

4.4. Custom Drive

The wave power surfaces procedure was also repeated with the custom drive installed, although gain and magnetic spring settings were restricted to those at or near the AC and DC electrical power optima so that a range of custom drive parameters could also be evaluated without substantially increasing the duration of the test. Because of the number of parameters that were varied, the number of points that would be presented in a given sliced surface are small may not be useful to evaluate overall trends. Instead, these results are presented as bar charts that show all parameter variations in a single figure.

Examining trends in custom drive DC power capture, it appears that decreasing switching frequency has the most noticeable effect on improving power capture (Figure 4-13). Increasing DC Bus voltage slightly decreases DC power capture. Increasing the velocity threshold does offer some marginal power capture improvements, but this effect is less significant and less consistent than decreased switching frequency. While it is beyond the scope of this document for a detailed analysis of custom drive findings, the conclusions presented here can be generalized somewhat. Inspection of Table 3-2 indicates that SVPWM was tested much more than the other switching modes: this was because

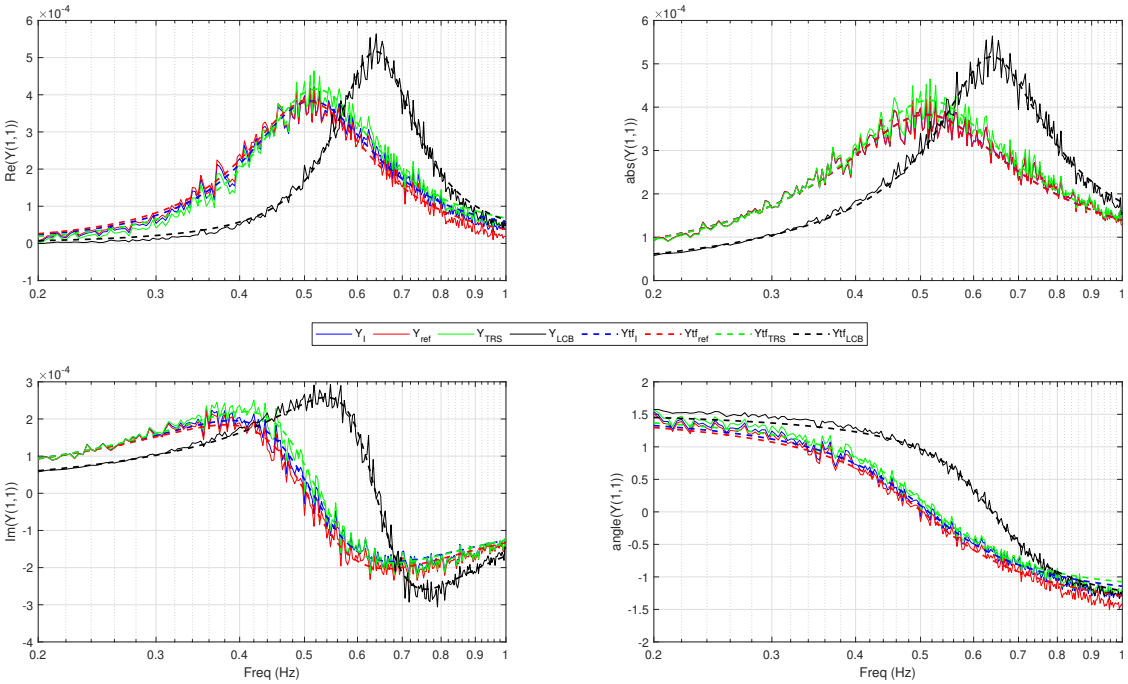

Figure 4-5. The real (top left), imaginary (bottom left), magnitude (top right), and phase (bottom right) of the frequency-domain admittance models for a magnetic spring rate of -9228 N/m. The force inputs are calculated from drive current (blue), commanded reference (red), measured from the heave TRS load cell (green), and the heave LCB load cell (black). Dotted lines indicate the fitted parametric transfer functions. This figure is made by `msSysIdentification1x1heave.m`.

it demonstrated superior performance over the other schemes, though varying switching scheme did not show the most significant performance differences of the tested parameters. Overall, the custom drive drastically improved DC power capture over the AMC drive.

The figure in this section is made from `makePowerSurfacesCD3.m` for the specified run. However, the test log should be consulted and the bar chart adjusted to apply this code to other custom drive tests, as the varied and relevant parameters depend on the drive switching algorithm.

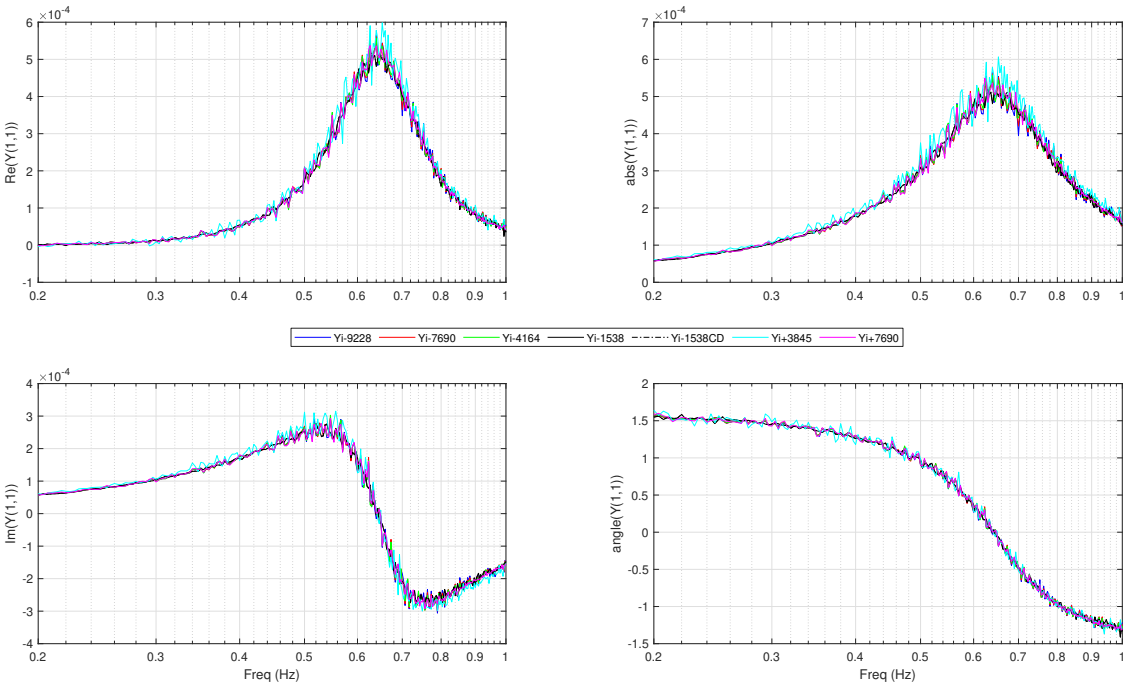

Figure 4-6. The real (top left), imaginary (bottom left), magnitude (top right), and phase (bottom right) of the frequency-domain intrinsic admittance model for all large-amplitude system ID runs. Note that these are not expected to vary with magnetic spring settings. This figure is made by aggregating models calculated from multiple runs of `msSysIdentification1x1heave.m`.

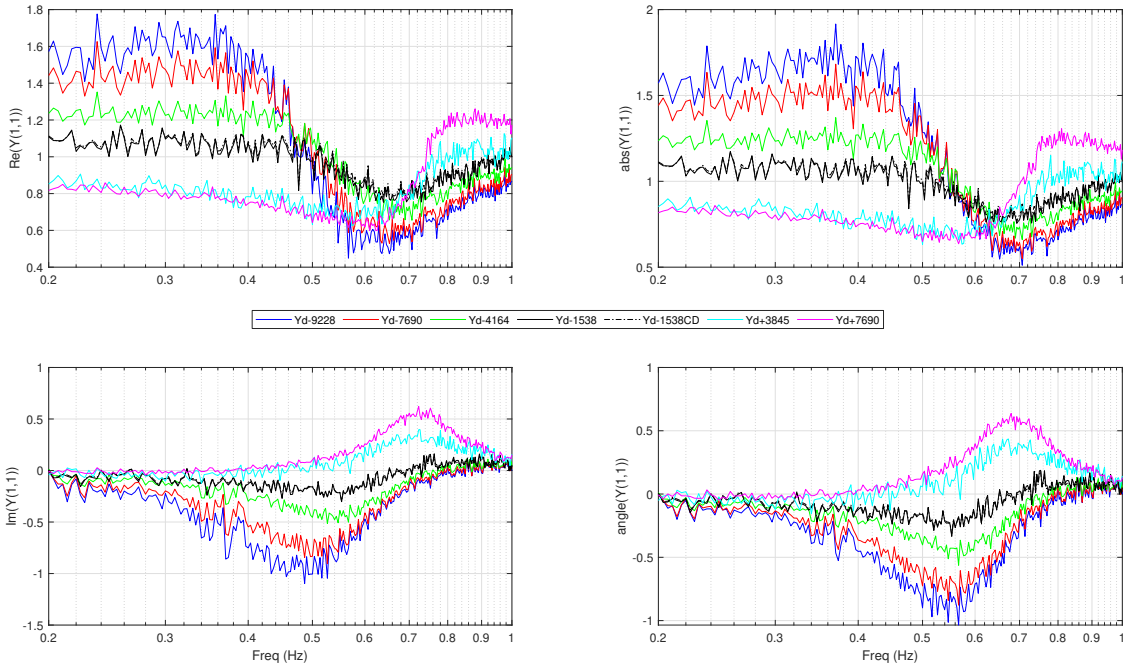

Figure 4-7. The real (top left), imaginary (bottom left), magnitude (top right), and phase (bottom right) of the frequency-domain drivetrain admittance model for all large-amplitude system ID runs. This model is expected to vary with magnetic spring settings. This figure is made by aggregating models calculated from multiple runs of `msSysIdentification1x1heave.m`.

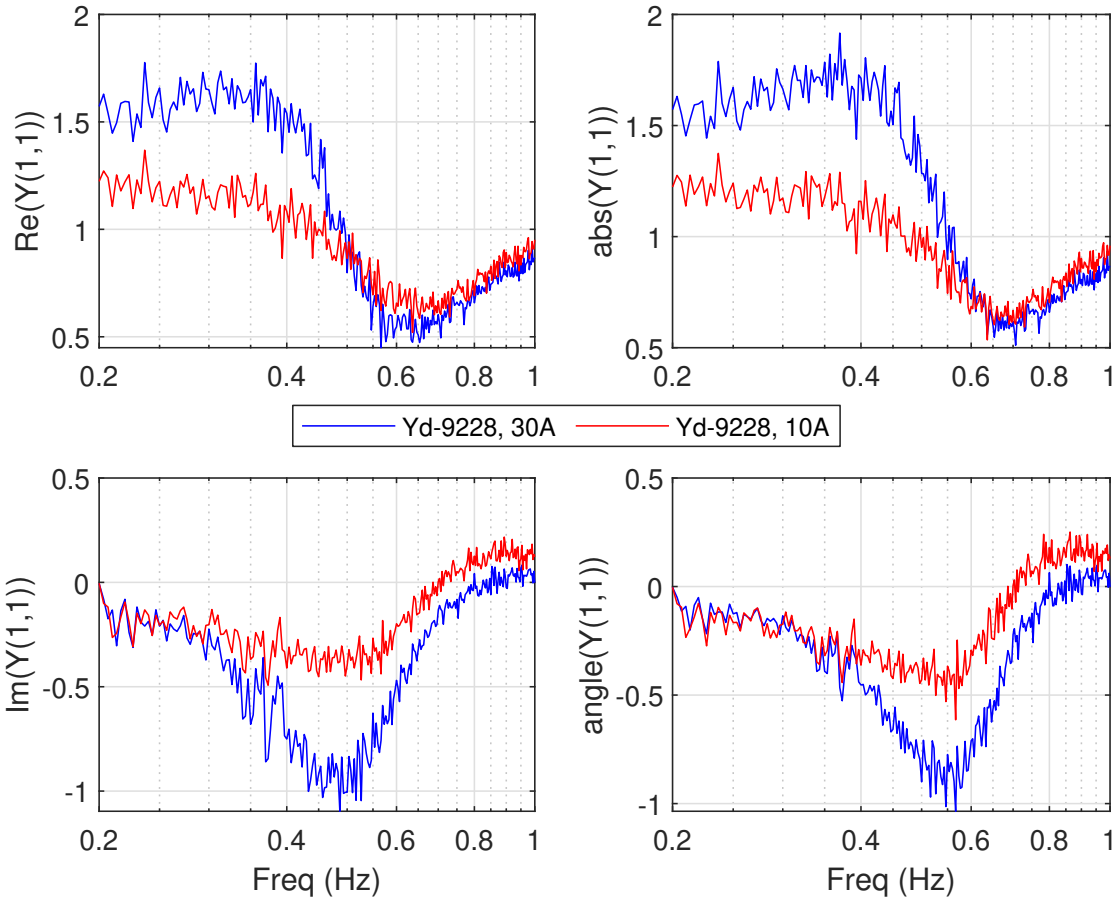

Figure 4-8. The real (top left), imaginary (bottom left), magnitude (top right), and phase (bottom right) of the frequency-domain drivetrain admittance model for the large (30 amp) and small (10 A) system identification test for a -9228 N/m spring rate. The distinction is attributable to the static friction acting significantly at the smaller amplitude. This figure is made by aggregating models calculated from multiple runs of `msSysIdentification1x1heave.m`.

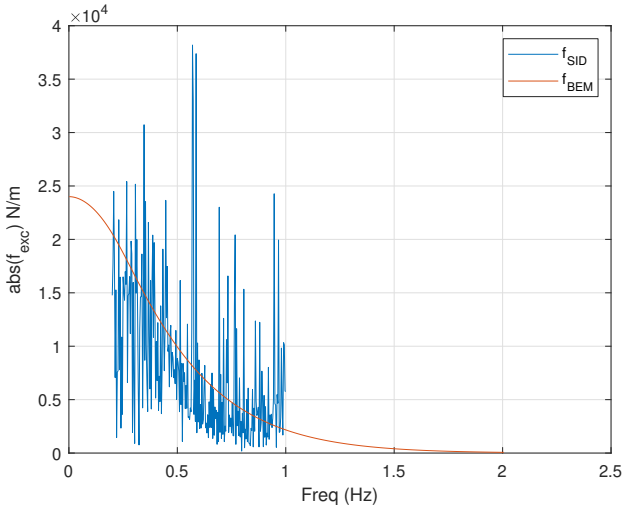

Figure 4-9. The non-parametric estimate of excitation from tank testing (f_{SID}), compared to the boundary-element method estimate (f_{BEM}).

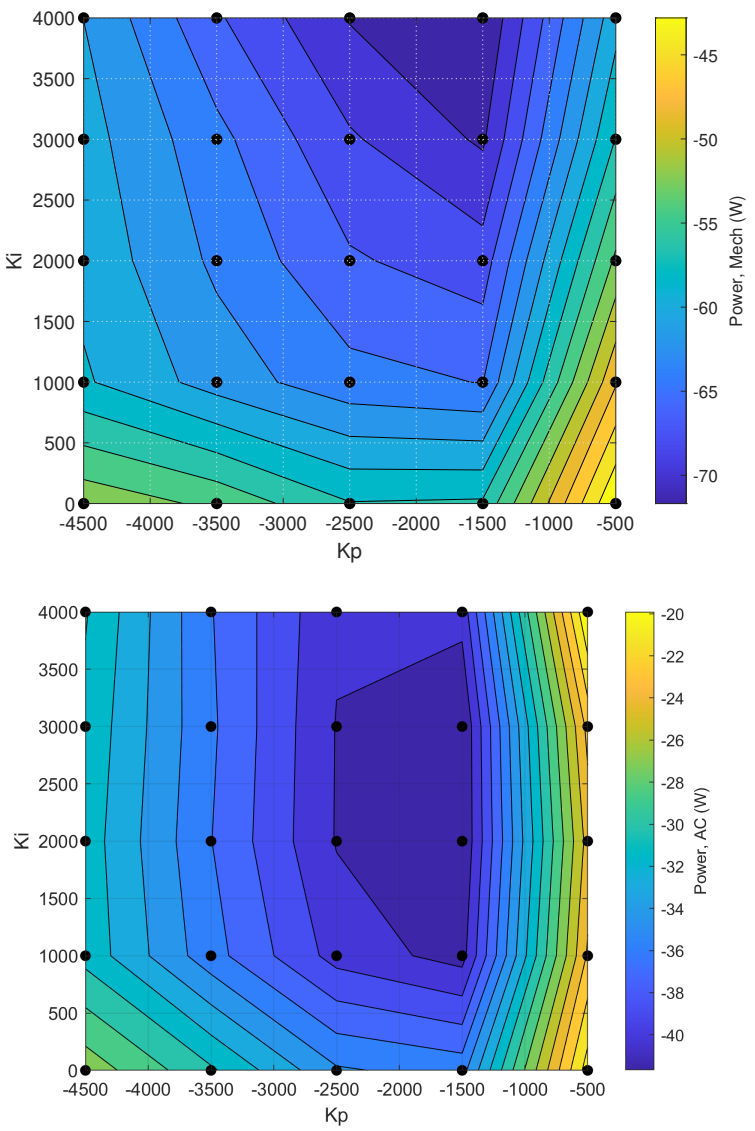

Figure 4-10. The mechanical power capture (top), AC power capture (bottom) for run 66, a 10 in JONSWAP wave with a 2.5 s peak period and a peak enhancement factor of 3.3. The contour surface is interpolated from data collected at the black points. This figure is made by `makePowerSurfacesv2.m`.

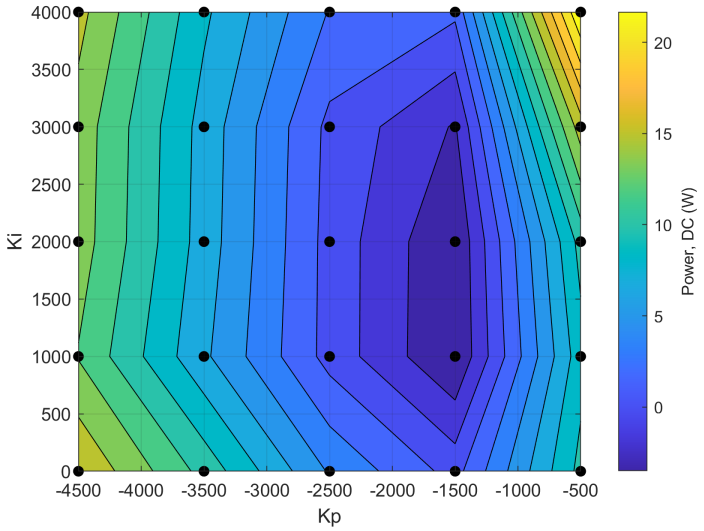

Figure 4-11. The DC power for run 66, a 10 in JONSWAP wave with a 2.5 s peak period and a peak enhancement factor of 3.3. The contour surface is interpolated from data collected at the black points. This figure is made by `makePowerSurfacesv2.m`.

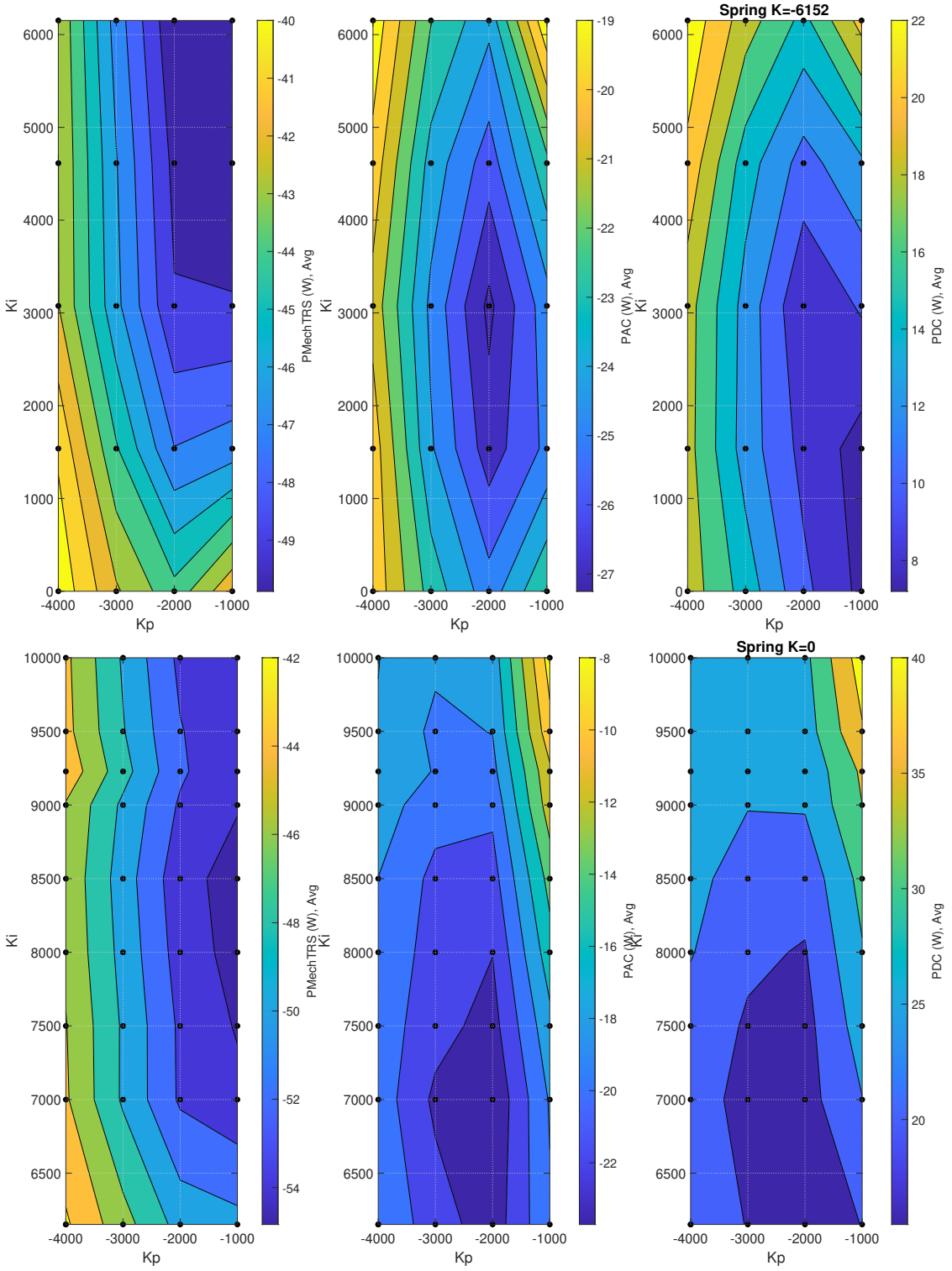

Figure 4-12. The mechanical power capture (left), AC power capture (middle), and DC power capture (right) for 2 different spring rates (top and bottom) for run 140, a 5 in regular wave with a 2 s period. The contour surface is interpolated from data collected at the black points: note the change in y-axis limits between the top and bottom plots. These figures are made by `makePowerSurfacesv2.m`.

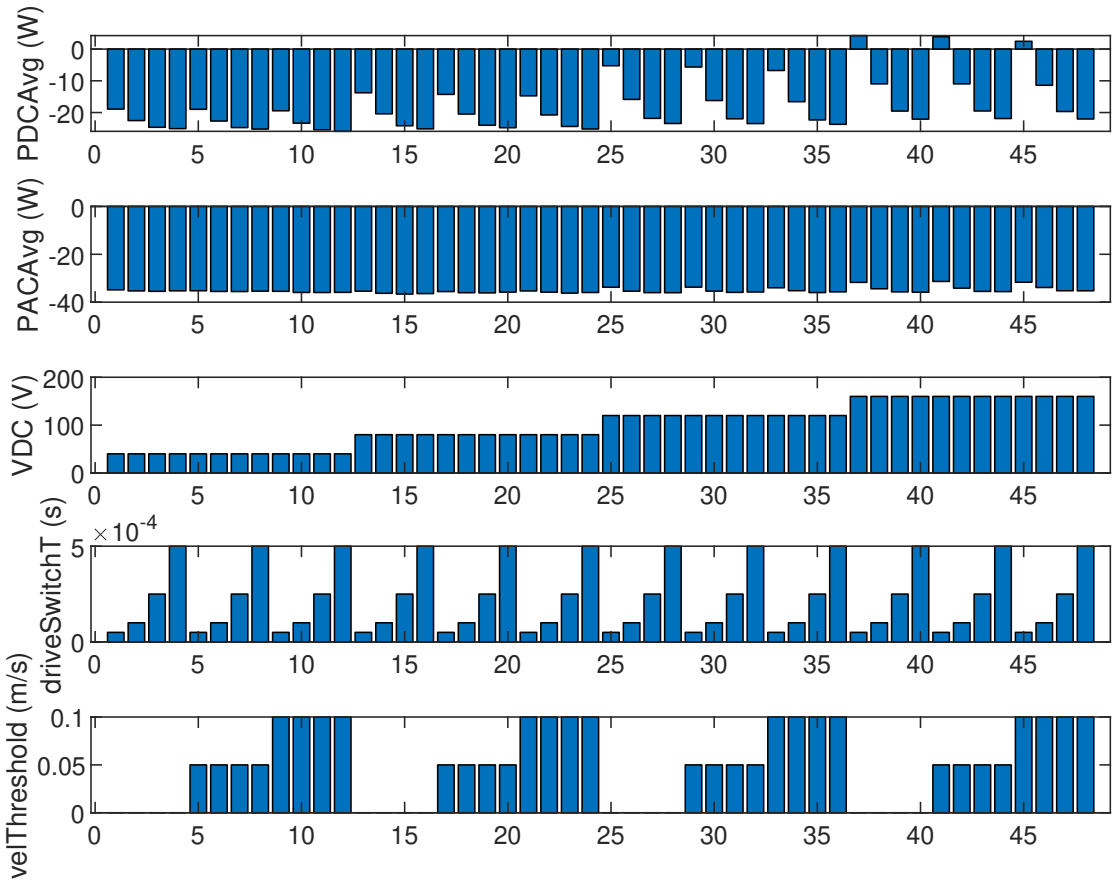

Figure 4-13. Bar plots of DC power (top), AC power (2nd from top), DC bus voltage set point (3rd), drive switching time (4th from top), and drive switching velocity threshold (bottom) for run 120, a 2.5 in 0.3 Hz regular wave. This figure is made from `makePowerSurfacesCD3.m`.

5. DISCUSSION

With a WEC proportional-integral controller and a tunable magnetic spring, there are three degrees of freedom an operator can manipulate to approach the impedance matching conditions at a given frequency. These two conditions can be expanded to four by examining the real and imaginary parts individually. Here, using Z_i and Z_d identified from the 30A system identification tests with no magnetic spring contribution, the effect of each tunable parameter on the impedance conditions can be considered (Figures 5-1 through 5-2)

The addition of the drivetrain stiffness degree of freedom delivered by the magnetic spring affects the imaginary part of the input impedance and both the real and imaginary parts of the output impedance. The controller allows adjustment of both the real and imaginary part of the load impedance and input impedance, but cannot alone attain both impedance matching conditions across all frequencies of interest. A drivetrain of a tunable stiffness expands the range of conditions over which this optima might be obtained, but this range is still limited. A further degree of freedom, for instance an adjustable gear ratio, would further this optimal tuning capability further. Practically, however, this flexibility in the in achieving optimal conditions must be balanced with the costs and physical limits (i.e., bounds on the achievable spring rates and range of rotation of the magnetic spring) of any added devices.

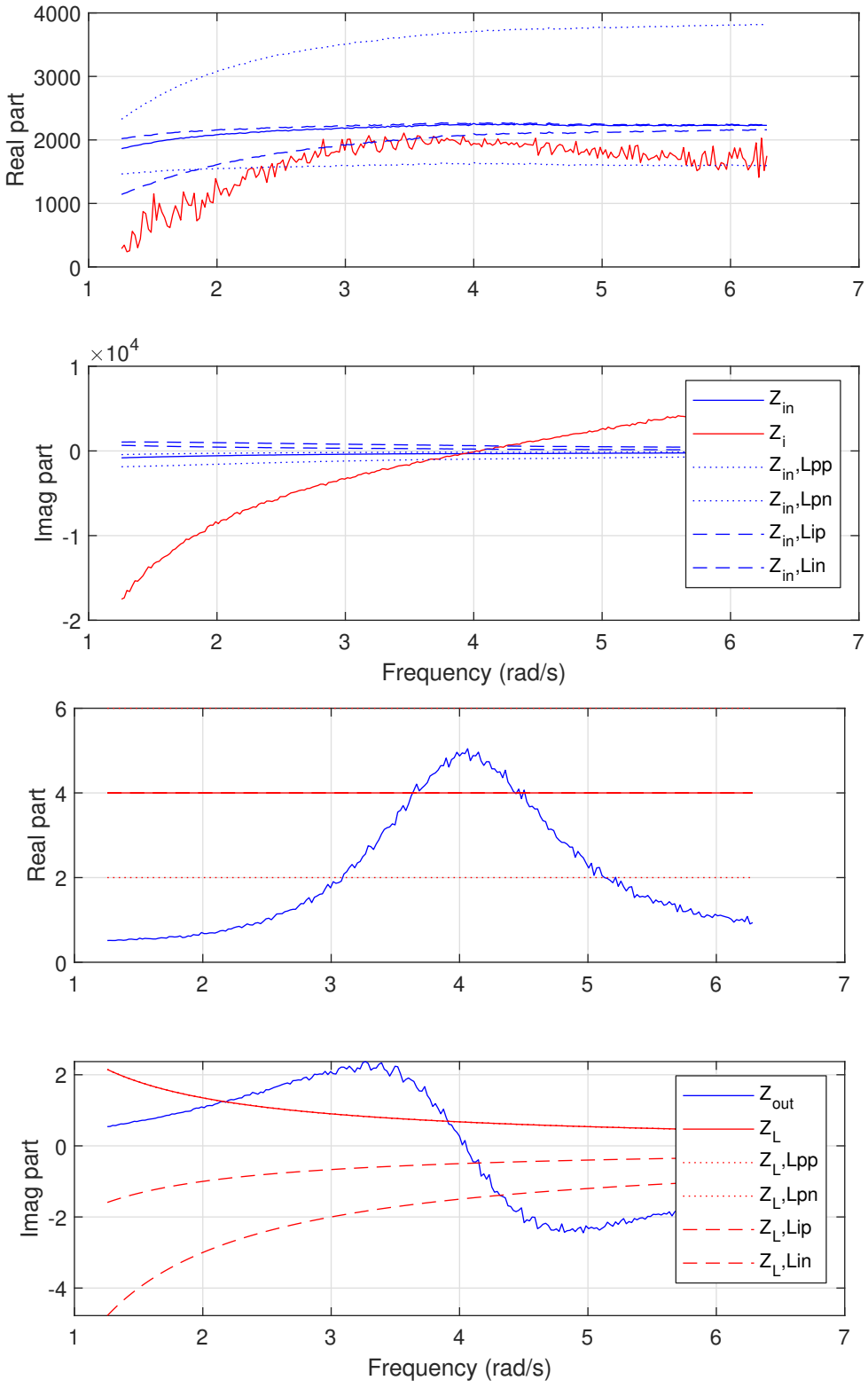

Figure 5-1. The effect of increasing (p) and decreasing (n) WEC controller proportional (p) and integral (i) gains on the input impedance (top) and load impedance (bottom).

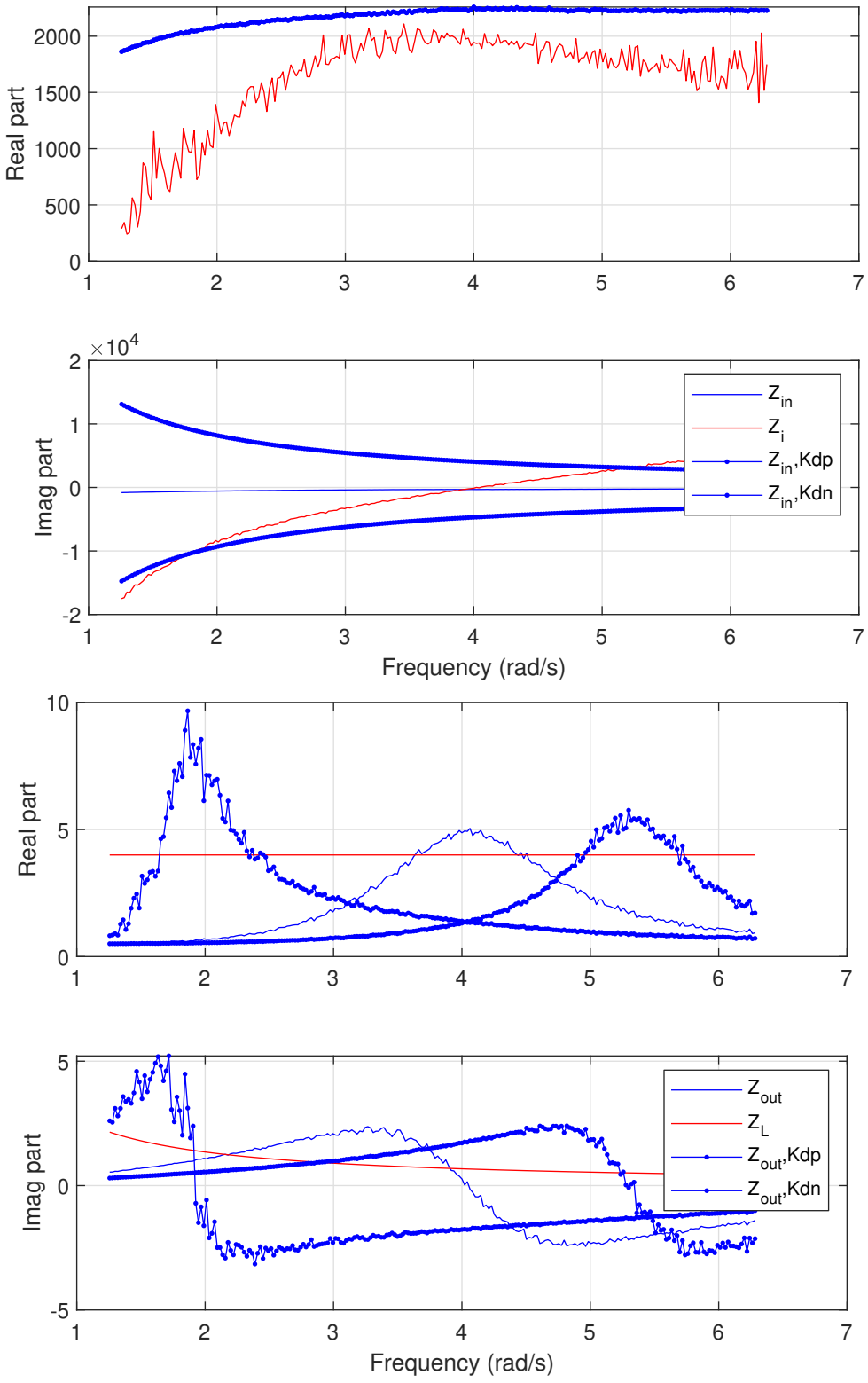

Figure 5-2. The effect of increasing (p) and decreasing (n) drivetrain (e.g., magnetic spring) stiffness gains on the input impedance (top) and output impedance (bottom).

6. CONCLUSION

The MASK4 test campaign evaluated the power-performance in multiple sea-states of a heave-actuated point absorber while varying its control parameters, drivetrain stiffness (including negative spring stiffness), and motor drive implementation. The ability to vary drivetrain stiffness via the magnetic spring system, though resulting in similar buoy dynamics as applying a similar negative spring term to the WEC controller, increased electrical power capture because it more closely met the bi-conjugate impedance matching criteria for optimal electrical power capture. However, it was still not possible to achieve these criteria generally in all investigated sea-states: as such, the optimal set of operating parameters were not obtained and instead a variety of equally sub-optimal parameter sets were located. This aligns well with the theory underlying the bi-conjugate impedance matching criteria, and validates this approach to WEC modeling, design, and optimization.

Additionally, particularly for periods of low power availability, intelligent control over motor drivers to reduce switching losses and parasitic power draw can have a significant impact. Of the investigated parameters, a reduction in drive switching frequency was found to be the most significant, followed by the introduction of a drive velocity threshold below which the motor drive ceases operation, thereby sharply reducing power draw during low-velocity motion when little power is available from the WEC. Practically, this implies that custom (or highly customizable off-the-shelf) motor drive options may offer significantly improved efficiencies for WECs.

Combined, this highlights areas of needed future research. Well-informed application of co-design approaches to WEC systems requires that a large, diverse amount of information is available at the outset, including novel actuation/device tuning modes to achieve or approximate bi-conjugate impedance matching criteria, the limitations of these methods, an understanding of physical component-level dynamics and performance, and, for commercial devices, an appropriate cost/power proxy of all of the above.

REFERENCES

[1] *Fully Controlled Three-Phase Bridge Converters*, chapter 12, pages 460–502. John Wiley & Sons, Ltd, 2013.

[2] Advanced Motion Controls. *DigiFlex Performance Servo Drive*, 2020.

[3] Giorgio Bacelli and Ryan G. Coe. WEC system identification and model validation. In *Proceedings of the 5th Marine Energy Technology Symposium (METS2017)*, Washington, D.C., 2017.

[4] Giorgio Bacelli and Ryan G. Coe. Comments on control of wave energy converters. *IEEE Transactions on Control Systems Technology*, 29(1):478–481, Jan 2021.

[5] Giorgio Bacelli, Ryan G. Coe, David Patterson, and David Wilson. System identification of a heaving point absorber: Design of experiment and device modeling. *Energies*, 10(10):472, 2017.

[6] Giorgio Bacelli, Steven J. Spencer, David C. Patterson, and Ryan G. Coe. Wave tank and bench-top control testing of a wave energy converter. *Applied Ocean Research*, 86:351 – 366, 2019.

[7] Dawei Che, Jonathan Z. Bird, Alex Hagmüller, and Md Emrad Hossain. An adjustable stiffness torsional magnetic spring with a linear stroke length. In *2021 IEEE Energy Conversion Congress and Exposition (ECCE)*, pages 5944–5948, 2021.

[8] Dawei Che, Bertrand Dechant, Alex Hagmüller, and Jonathan Z. Bird. A multi-stack variable stiffness magnetic torsion spring for a wave energy converter. In *2022 IEEE Energy Conversion Congress and Exposition (ECCE)*, pages 1–6, 2022.

[9] Hancheol Cho, Giorgio Bacelli, and Ryan G Coe. Linear and nonlinear system identification of a wave energy converter. In *Proceedings of the 4th Marine Energy Technology Symposium (METS2016)*, Washington, D.C., 2018.

[10] Hancheol Cho, Giorgio Bacelli, and Ryan G. Coe. Model predictive control tuning by inverse matching for a wave energy converter. *Energies*, 12(21):4158, Oct 2019.

[11] Hancheol Cho, Giorgio Bacelli, Victor Nevarez, Felipe Wilches-Bernaland, and Ryan G. Coe. Evaluation of predictionless control for wave energy converters. In *Proceedings of the 13th European Wave and Tidal Energy Conference (EWTEC2019)*, Napoli, Italy, September 2019.

[12] Dae-Woong Chung, Joohn-Sheok Kim, and Seung-Ki Sul. Unified voltage modulation technique for real-time three-phase power conversion. *IEEE Transactions on Industry Applications*, 34(2):374–380, 1998.

[13] Ryan G. Coe and Giorgio Bacelli. A summary of the Advanced WEC Dynamics and Control project. Technical Report SAND2019-14355, Sandia National Laboratories, Albuquerque, NM, Nov 2019.

[14] Ryan G. Coe, Giorgio Bacelli, David Patterson, and David G. Wilson. Advanced WEC Dynamics & Controls FY16 testing report. Technical Report SAND2016-10094, Sandia National Labs, Albuquerque, NM, October 2016.

[15] Ryan G. Coe, Giorgio Bacelli, Steven J. Spencer, and Hancheol Cho. Initial results from wave tank test of closed-loop WEC control. Technical Report SAND2018-12858, Sandia National Laboratories, Albuquerque, NM, Nov 2018.

[16] Ryan G. Coe, Giorgio Bacelli, Steven J. Spencer, Dominic Forbush, and Kevin Dullea. Advanced WEC dynamics and controls MASK3 test. Technical Report SAND2019-15428, Sandia National Laboratories, Albuquerque, NM, Dec 2019.

[17] Johannes Falnes. *Ocean Waves and Oscillating Systems*. Cambridge University Press, Cambridge; New York, 2002.

[18] Jeff T. Grasberger, Ryan G. Coe, Jonathan Bird, Giorgio Bacelli, Alex Hagmüller, and Carlos Michelén Ströfer. Maximizing wave energy converter power extraction by utilizing a variable negative stiffness magnetic spring. In *Proceedings of the 15th European Wave and Tidal Energy Conference (EWTEC2023)*, Bilbao, Spain, September 2023.

[19] Andrew Hamilton, François Cazenave, Dominic Forbush, Ryan G. Coe, and Giorgio Bacelli. The MBARI-WEC: a power source for ocean sensing. *Journal of Ocean Engineering and Marine Energy*, 7(2):189–200, 2021.

[20] Md Emrad Hossain, Jonathan Z. Bird, Victor Albarran, and Dawei Che. Analysis and experimental testing of a new type of variable stiffness magnetic spring with a linear stroke length. In *2021 IEEE Energy Conversion Congress and Exposition (ECCE)*, pages 5961–5965, 2021.

[21] Carlos A Michelén Ströfer, Ryan G. Coe, et al. Control co-design and uncertainty analysis of the LUPA's PTO using WecOptTool. In *Proceedings of the 15th European Wave and Tidal Energy Conference (EWTEC2023)*, Bilbao, Spain, September 2023.

[22] Taraz Technologies. *40kW Three Phase Inverter Stack*, 2015.

[23] Madelyn G. Veurink, Wayne W. Weaver, Rush D. Robinett, David G. Wilson, Giorgio Bacelli, and Ryan G. Coe. Wave energy converter direct drive power-take-off power electronic design to maximize power production. In *2023 IEEE 24th Workshop on Control and Modeling for Power Electronics (COMPEL)*, pages 1–7, Ann Arbor, MI, June 2023. IEEE.

DISTRIBUTION

Email—Internal

Name	Org.	Sandia Email Address
Technical Library	1911	sanddocs@sandia.gov

Sandia National Laboratories

Sandia National Laboratories is a multimission laboratory managed and operated by National Technology & Engineering Solutions of Sandia LLC, a wholly owned subsidiary of Honeywell International Inc., for the U.S. Department of Energy's National Nuclear Security Administration under contract DE-NA0003525.